1. REPORT DATE (DD-MM-YYYY) September 2012	2. REPORT TYPE Journal Article	3. DATES COVERED (From - To) September 2012-September 2012
4. TITLE AND SUBTITLE Exploring the structure of nitrogen-rich ionic liquids and their binding to the surface of oxide-free boron nanoparticles		5a. CONTRACT NUMBER IN-HOUSE
		5b. GRANT NUMBER
		5c. PROGRAM ELEMENT NUMBER
6. AUTHOR(S) JPL Perez, BW McMahon, S Schneider, JA Boatz, TW Hawkins, PD McCrary, PA Beasley, SP Kelley, RD Rogers SL Anderson		5d. PROJECT NUMBER
		5e. TASK NUMBER
		5f. WORK UNIT NUMBER Q0C5
7. PERFORMING ORGANIZATION NAME(S) AND ADDRESS(ES) Air Force Research Laboratory (AFMC) AFRL/RQRP 10 E. Saturn Blvd. Edwards AFB, CA, 93524-7680		8. PERFORMING ORGANIZATION REPORT NO.
9. SPONSORING / MONITORING AGENCY NAME(S) AND ADDRESS(ES) Air Force Research Laboratory (AFMC) AFRL/RQR 5 Pollux Dr. Edwards AFB, CA, 93524-7048		10. SPONSOR/MONITOR'S ACRONYM(S)
		11. SPONSOR/MONITOR'S REPORT NUMBER(S) AFRL-RQ-ED-JA-2012-279
12. DISTRIBUTION / AVAILABILITY STATEMENT Approved for public release; distribution unlimited		

14. ABSTRACT

The structure of two different energetic ionic liquids and the nature of their binding to elemental boron surfaces were investigated by a combination of X-ray photoelectron spectroscopy, IR spectroscopy, zeta potential measurements, thermogravimetric analysis, and first-principles theory. It was found that both 1-methyl-4-amino-1,2,4- triazolium dicyanamide ([MAT][DCA]) and 1-butyl-3-methylimidazolium dicyanamide ([BMIM][DCA]) ionic liquids bind to boron well enough to resist removal by ultrasonic washing and to protect the boron surface from oxidation during air exposure of the washed powder. The data suggest that both the cation and the anion of the ionic liquids interact with the boron surface; however, for [MAT][DCA], the interaction of the cation appears to dominate, while for [BMIM][DCA] the interaction with the [DCA]- anion dominates. The difference is attributed to the binding of boron to the amino group of [MAT]+, and the amino group also appears to help bind a thicker ionic liquid (IL) capping layer.

15. SUBJECT TERMS

16. SECURITY CLASSIFICATION OF:			17. LIMITATION OF ABSTRACT	18. NUMBER OF PAGES	19a. NAME OF RESPONSIBLE PERSON Wayne Kalliomaa
a. REPORT Unclassified	b. ABSTRACT Unclassified	c. THIS PAGE Unclassified	SAR	16	19b. TELEPHONE NO (include area code) 661-275-6442

Exploring the Structure of Nitrogen-Rich Ionic Liquids and Their Binding to the Surface of Oxide-Free Boron Nanoparticles

Jesus Paulo L. Perez,[†] Brandon W. McMahon,[†] Stefan Schneider,[‡,∥] Jerry A. Boatz,[‡,∥] Tom W. Hawkins,[‡,∥] Parker D. McCrary,[§] Preston A. Beasley,[§] Steven P. Kelley,[§] Robin D. Rogers,[§,∥] and Scott L. Anderson[†,∥,]*
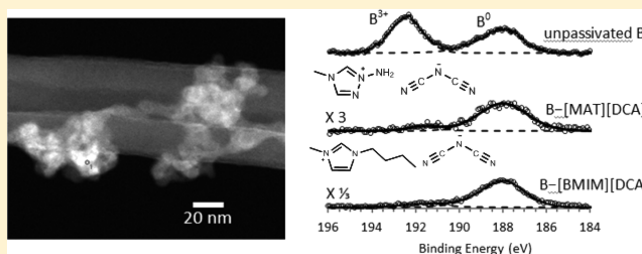
[†]Department of Chemistry, University of Utah, 315 South 1400 East, Salt Lake City, Utah 84112, United States

[‡]Propellants Branch, Rocket Propulsion Division, Aerospace Systems Directorate, Air Force Research Laboratory, AFMC AFRL/RQRP, 10 East Saturn Boulevard, Edwards AFB, California 93524, United States

[§]Center for Green Manufacturing and Department of Chemistry, The University of Alabama, Tuscaloosa, Alabama 35487, United States

Ⓢ *Supporting Information*

ABSTRACT: The structure of two different energetic ionic liquids and the nature of their binding to elemental boron surfaces were investigated by a combination of X-ray photoelectron spectroscopy, IR spectroscopy, zeta potential measurements, thermogravimetric analysis, and first-principles theory. It was found that both 1-methyl-4-amino-1,2,4-triazolium dicyanamide ([MAT][DCA]) and 1-butyl-3-methylimidazolium dicyanamide ([BMIM][DCA]) ionic liquids bind to boron well enough to resist removal by ultrasonic washing and to protect the boron surface from oxidation during air exposure of the washed powder. The data suggest that both the cation and the anion of the ionic liquids interact with the boron surface; however, for [MAT][DCA], the interaction of the cation appears to dominate, while for [BMIM][DCA] the interaction with the [DCA]⁻ anion dominates. The difference is attributed to the binding of boron to the amino group of [MAT]⁺, and the amino group also appears to help bind a thicker ionic liquid (IL) capping layer.

I. INTRODUCTION

Hydrazine and its derivatives are widely employed as propellants in rocket engines for spacecraft station keeping, orbit maneuvering, and orientation control applications. A typical bipropellant rocket engine might use a hydrazine compound as fuel and nitrogen tetroxide (NTO) as oxidizer.[1] The fact that such mixtures are hypergolic (i.e., they spontaneously ignite upon mixing) has important advantages in propulsion applications; however, hydrazine and its derivatives have serious disadvantages, including high vapor pressure with toxic[2,3] and flammable vapors and relatively low energy density.[1,2] Ionic liquids (ILs), now defined as salts with melting point below 100 °C, can have low or negligible vapor pressures, and the wide variety of cations and anions available make it possible to tune the properties for a wide variety of applications.[4−10] The discovery of ILs with hypergolic properties opened the possibility of using them as low vapor pressure, safer rocket propellants.[11−15] Throughout the years, researchers at the Air Force Research Laboratory (AFRL) have synthesized hypergolic ILs, focusing on imidazolium-based cations for their stability in air and also for high nitrogen content and dicyanamide[12,13,15] and dicyanoborate[16] anions for lower viscosity[17,18] and better ignition delay properties, respectively. Also, such propellants can potentially have significantly higher

energy density than those of hydrazine and its derivatives. Shreeve et al. synthesized a number of highly energetic ionic liquids with multiple nitrogen atoms in their structures,[18−23] in the hope of increasing volumetric and gravimetric energy density by introducing multiple nitrogen atoms and more nitrogen−nitrogen bonds.[24−27] In lieu of this, azolium azolate ILs, salts with both cation and anion composed of heterocyclic organic ions, are now being considered as the next stage in IL propellant development, although their hypergolic property is yet to be demonstrated.[28−34] A more detailed review of some of the considerations involved in developing IL propellants is given in the Supporting Information (SI).

In addition to developing improved ILs, another approach to increase energy density is adding high energy density nanoparticles to the IL propellant. Boron has both gravimetric (59.0 MJ/kg) and volumetric (137.8 MJ/L) energy densities[35] that are far higher than those for typical hydrocarbons (35−40 MJ/L or kg) and significantly higher than those of other active metal fuels such as aluminum (31.0 MJ/kg, 83.8 MJ/L)[35] or magnesium (24.0 MJ/kg, 43.0 MJ/L).[35] Therefore, boron

nanoparticles have attracted significant interest as additives to liquid fuels and propellants.[36−43]

Boron's potential as a high energy fuel additive is impeded by its high vaporization temperature, which results in oxidation being a heterogeneous process, and thus limited by the diffusion of reactants and products to and from the interface. Furthermore, boron, like most active metals, develops a thin, passivating oxide layer upon air exposure, and this oxide layer inhibits ignition under combustion conditions.[37,38] Using boron in the form of well-dispersed nanoparticles increases the surface area and mitigates the diffusion limitation; however, the oxide layer still inhibits particle ignition and also makes up an increasing fraction of the particle mass as the dimension is reduced.[41] Therefore, a possible strategy for improving the ignition properties of boron (or any metal particle) is to cap the nanoparticles with chemical agents that prevent formation of the passivating oxide layer and also render the particles highly dispersible in the fuel of interest.[44,45]

We have previously shown that unoxidized, air-stable boron nanoparticles capped with oleic acid can be synthesized by ball milling and are highly dispersible in hydrocarbon fuels.[44,45] The oleic acid layer is expected to desorb or oxidize at relatively low temperatures, allowing ignition of the underlying unoxidized boron. Also, we recently demonstrated that a similar approach can be used to generate unoxidized and air-stable boron nanoparticles by capping with a hypergolic IL, [MAT][DCA].[46] Additionally, these boron nanoparticles do not inhibit hypergolic ignition of the IL with nitric acid.[47]

An important issue in generalizing this result to other ILs or other metals is the lack of understanding of the nature of the IL−boron bonding. This information would also be useful in understanding issues like IL storability and stability in contact with metals. In this paper, we report the spectroscopic studies on neat [MAT][DCA] and [BMIM][DCA] ILs, as well as their interactions with boron surfaces. In addition, light scattering, thermogravimetric, and quantum chemistry techniques were utilized to probe the boron−IL systems.

II. EXPERIMENTAL AND COMPUTATIONAL METHODOLOGY

A. Boron Milling Process. Boron powder (97%, ∼2 μm nominal particle size) from C.R. Supply Co. (West Hills, CA) was used as starting material in the milling process. The [MAT][DCA] and [MAT]I ILs used were synthesized at the Air Force Research Laboratory (AFRL) at Edwards AFB, using procedures described elsewhere.[13] [BMIM]Cl was synthesized through a neat quaternization reaction between 1-methyl-imidazole, redistilled prior to use, and 1-chlorobutane, which were purchased from Sigma-Aldrich (St. Louis, MO). [BMIM]-[DCA] and Na[DCA] were purchased from Sigma Aldrich and used as received. Ethanol (200 proof) and acetonitrile (99.5%) solvents were purchased from PharmCo-Aaper Products Inc. (Brooksfield, CT) and Macron, Inc. (San Antonio, TX), respectively. Air-sensitive reagents were handled and stored in a N$_2$-filled glovebox. Particle size reduction was done using a small-scale shaker mill (Spex, (Metuchen, NJ) Certiprep 8000 model) using a 55-mL tungsten carbide-lined milling jar with tungsten carbide media, following a procedure described previously[46] and summarized here. A two-stage milling process was employed. First, 1.0 g of boron was dry milled with 80.0 g of 1/8 inch tungsten carbide balls for one hour. To avoid possible reaction of boron with nitrogen under milling conditions, the dry milling was done under Ar atmosphere by

loading and sealing the jar in an Ar-filled glovebox. This "dry milling" process accomplishes part of the particle size reduction and thereby produces a substantial area of fresh unoxidized boron surface that is highly reactive. At this point, the jar was opened, and 10.0 mL of the IL was added prior to milling for an additional three hours. After milling, the boron/IL mixture was scraped out of the jar and washed off the balls using ethanol as solvent. Opening and closing of the milling jar for addition of reagents were done inside the Ar-filled glovebox.

Hazards. Unpassivated boron nanoparticles are highly pyrophoric, and exposure to air leads to spontaneous ignition, which can be violent for dry particles. Ignition can occur after a substantial delay if the particles are wet at the time of exposure. While the milling procedures described produce air-stable boron nanoparticles, as a safety measure we always treat the particles as if they are pyrophoric until they have been proven to be air-stable by testing on small samples. In addition, any materials such as solvents, paper towels, sample bottles, etc. that have been in contact with boron nanoparticles must be treated as potentially pyrophoric. Before disposing such potentially contaminated items, they were exposed to air in a fume hood for several days to ensure time for oxygen to diffuse and react with any unpassivated boron present.

B. Size Characterization. Particle size and size distributions were analyzed using scanning electron microscopy (SEM-FEI Nova Nano 600, Hillsboro, OR) and dynamic light scattering (DLS—Wyatt DynaPro NanoStar, Wyatt Technology, Dernbach, Germany), respectively. Samples for SEM were washed by sonicating the particles with ethanol and centrifuging. The centrifuged particles were redispersed in fresh ethanol, and the process was repeated for a total of three washings to remove any ILs that are not bound to the particle surface, as these tend to cause adverse charging artifacts during SEM analysis. Washed particles were diluted with ethanol, then drop casted and dried on a transmission electron microscopy (TEM) grid, and affixed on a SEM aluminum stub using carbon tape. DLS analysis was done on washed samples diluted and dispersed in ethanol.

C. X-ray Photoelectron Spectroscopy (XPS). XPS analyses were done using a Kratos Axis Ultra instrument (Chestnut Ridge, NY). For XPS of the ionic liquid itself, a drop of neat [MAT][DCA] or [BMIM][DCA] was placed in a shallow well, machined in an aluminum sample holder fabricated to handle liquid samples. The sample-containing well was clamped on a Kratos sample bar and placed inside the load lock of the instrument and evacuated before transfer into the ultrahigh vacuum (UHV) system. The vapor pressures of both ILs are low enough that no significant pressure rise was observed after introduction of the IL samples. For boron samples, XPS was done on as-milled nanoparticles in excess IL and also on boron recovered at various stages of the ethanol washing process, described above. The washed samples were dried in air overnight to evaporate ethanol and then pressed onto a carbon tape atop a copper shim, prior to introduction into the XPS instrument's vacuum system.

X-ray photoelectron spectra were taken using the monochromatic Al Kα source (1486.7 eV) at a 300 × 700 μm spot size. Low-resolution survey and high-resolution region scans were taken for each sample. To minimize charging, samples were flooded with low-energy electrons and ions from the instrument's built-in charge neutralizer. Data were analyzed using CASA XPS software, and energy corrections on high-resolution scans were done by referencing the C 1s peak of

adventitious carbon to 284.5 eV.[48] As shown below, this energy referencing method gives literature-consistent binding energies for boron as well.

D. Fourier Transform Infrared (FTIR) Spectroscopy. Infrared (IR) spectra were collected using a Bruker (Madison, WI) platinum α-FTIR by direct measurement via attenuated total reflectance of samples on a diamond crystal. Solid nanoparticulate samples were washed with ethanol to remove unbound ILs, air-dried, and then pressed onto a diamond crystal with a Platinum ATR QuickSnap sampling module. Spectra were acquired with resolution of 1 cm^{-1} in 10 independent scans and then averaged.

E. Zeta Potential Measurements. Zeta potentials were measured using a Particle Sizing Systems NICOMP 380 instrument (Santa Barbara, CA). Dried, ethanol-washed boron nanoparticles were dispersed in acetonitrile (Macron Chemicals, San Antonio, TX, 99.8%). Acetonitrile was used as solvent to eliminate any possibility of hydrolysis of ethanol or water on the boron nanoparticle surface. Measurements were made at three different applied potentials (5, 10, and 15 mV/cm^2), and because the zeta potentials were independent of the applied potential within the uncertainty, the values were averaged. The calibration of the NICOMP instrument was checked by measuring the zeta potential of a zeta potential standard sample, which was also measured on a Zetasizer Nano Z instrument (Malvern Instruments Ltd., Worcestire, UK).

F. Thermogravimetric Analysis (TGA). A TGA 2950 Thermogravimetric Analyzer (TA Instruments, New Castle, DE) was used to measure mass changes occurring during heating of the ILs and IL-functionalized boron. Neat ILs were run at a temperature ramp rate of 20 °C/min from 35 to 800 °C under O$_2$. Boron samples were run at a slower ramp rate of 5 °C/min from 35 to 900 °C also under O$_2$ atmosphere. The slower ramp rate and increased range for boron nanoparticles were used because full oxidation of the solid samples is expected to be limited by diffusion of oxygen through the boron oxide layer that initially forms as the IL is desorbed/decomposed.

G. Core-Level Binding Energies and Charge Distribution Calculations. Density functional theory (DFT) calculations were performed using the revised Tao−Perdew−Staroverov−Scuseria (revTPSS) meta-generalized gradient approximation (meta-GGA) functional[49] and the 6-311++G(d,p) basis set.[50−52] All structures were fully optimized and verified as local minima by confirming that the Hessian matrix is positive definite, i.e., that the calculated harmonic vibrational frequencies are all real. All calculations were performed using the GAMESS[53,54] quantum chemistry package. Calculated core level orbital energies were used as an approximation of the binding energies to be expected for ionizing out those levels. Because this approximation (Koopmans' theorem: binding energy = −orbital energy)[55] neglects relaxation and screening, the orbital energies differ substantially from the experimental binding energies. Differences between orbital energies for different atomic centers are, however, expected to mirror the differences in measured binding energies. For the comparisons given below, the Koopmans' theorem binding energies were shifted to bring the calculated and experimental binding energies for the most strongly bound orbital into agreement but were not scaled or otherwise corrected.

III. RESULTS AND DISCUSSION

The ultimate goal of this study is to understand how the two ILs form dense, solvent-resistant passivating layers on boron; however, interpreting the spectroscopic data regarding IL−boron binding requires that we first understand the spectroscopic signature of the ionic liquids. The results are interesting in themselves, because they provide insight into the structure and charge distributions in the neat ILs.

A. XPS Analysis of Liquid [MAT][DCA] and [BMIM][DCA]. A number of researchers have taken advantage of the low vapor pressure of ILs to measure the C 1s, N 1s, O 1s, and S 2p X-ray photoelectron spectra (XPS) of various ILs, correlating the observed core level binding energies to the ILs' structures.[56−60] These analyses relied on binding energy values from other compounds with fragments that were isostructural to the ILs studied. Here we took advantage of the fact that the XPS for the ILs of interest show considerable structure that could be compared to ab initio theory to make assignments. The assignments were confirmed by reference studies on salts containing either the cation or anion of interest. For instance, 1-methyl-4-amino-1,2,4-triazolium iodide ([MAT]I) and 1-butyl-3-methyl-imidazolium chloride ([BMIM]Cl) were used as references to identify the N 1s and C 1s XPS signals coming from [MAT]$^+$ and [BMIM]$^+$ cations, respectively, while sodium dicyanamide (Na[DCA]) was used for the [DCA]$^-$ anion.

Figure 1a shows the high-resolution N 1s spectra for [MAT]I (broken line) and Na[DCA] (solid line) plotted together to allow direct comparison with the N 1s spectrum for the [MAT][DCA] IL (Figure 1b). The [MAT]$^+$ cation has four N atoms, all of which are unique and distinguishable, at least in principle. The [DCA]$^-$ anion has a central N atom and a pair of terminal N atoms that are equivalent at least in the isolated anion. This equivalence results in exact overlaying of the two fit components that make up the terminal N peak. The structures of the cations and anions and the labels used for the different N atoms are shown in Figure 1e. The spectra were fit by assuming that there should be four component peaks for [MAT]I and three for Na[DCA] (with the two N$_{DT}$ atoms being identical), each with the same integrated intensity. The peak positions and widths of the fit components were allowed to be freely adjustable, resulting in excellent fits. The best-fit widths of the components are all about the same, with the exception of that for N$_{DC}$ (the central N atom in [DCA]$^-$), which is best fit with a somewhat narrower peak indicating a more homogeneous environment for the central N atom. It is clear from these spectra that the four N atoms in [MAT]$^+$ have higher N 1s binding energies than any of the N atoms in [DCA]$^-$, which is consistent with the usual idea that positively charged centers should have chemical shifts to higher binding energies, while negatively charged centers should have chemical shifts to lower binding energies.

In the case of [DCA]$^-$, symmetry allows assignment of the weaker peak at 399.6 eV to the central N atom (N$_{DC}$) and the stronger peak (twice the integrated intensity) at 398.3 eV to the two terminal N atoms (N$_{DT}$). The implication is that the negative charge on the anion is largely distributed between the nitrile groups, leaving the central N atom with a smaller negative charge than the two terminal N atoms. For [MAT]$^+$, the four N atoms clearly fall into two distinct pairs of chemical shifts; however, a more detailed assignment of the individual N atoms to the two spectral features is not possible, a priori.
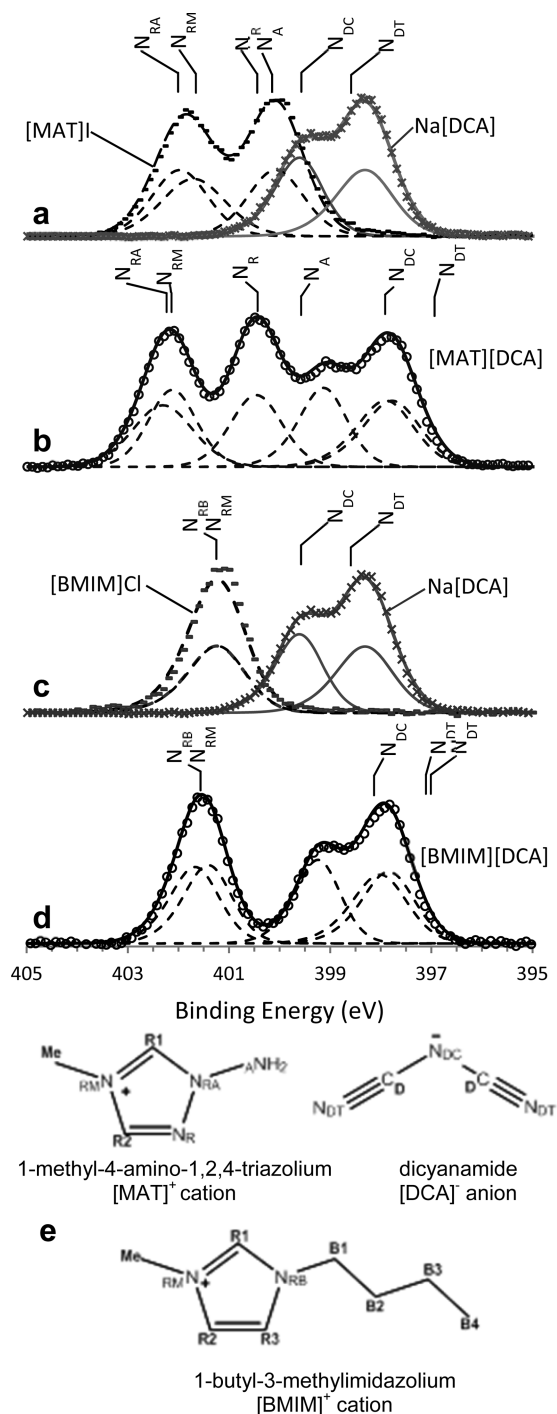
Figure 1. N 1s high-resolution XPS scan of (a) [MAT]I and Na[DCA] (overlapped), (b) [MAT][DCA], (c) [BMIM]Cl and Na[DCA] (overlapped), and (d) [BMIM][DCA]. (e) Chemical structures of the IL cation and anion.

Clearly, the overlapped spectra of [MAT]I and Na[DCA] are quite similar to the N 1s spectrum of neat [MAT][DCA], indicating that local environments around [MAT]$^+$ and [DCA]$^-$ are similar in the IL and in the two salts examined. From the comparison, it is clear that the two higher binding energy peaks at 402 and 400 eV in the spectrum of [MAT][DCA] must correspond to the nitrogen atoms of [MAT]$^+$, while the two low binding energy peaks at 399 and 398 eV must result from [DCA]$^-$. Likewise, the N 1s spectrum

of [BMIM][DCA] is well represented by overlapping the spectra of [BMIM]Cl and Na[DCA], making it clear that in the [BMIM][DCA] spectrum (Figure 1d) the two low binding energy peaks come from the three N atoms in [DCA]$^-$, while the high binding N 1s signal at 402 eV must correspond to overlapping contributions from the two N atoms in the [BMIM]$^+$ cation.

To assign the spectra in detail, we carried out DFT calculations on single ion pairs of both ILs and on the reference compounds, [MAT]I, [BMIM]Cl, and Na[DCA], determining N 1s and C 1s core orbital energies and atomic charges. As described above, these were shifted to correct for relaxation and screening effects not included in the calculations and compared with the experimental binding energies. The theoretical N 1s binding energies are indicated in the figure as vertical lines labeled according to the scheme in Figure 1e. Table 1 lists the experimental and theoretical N 1s binding

Table 1. N 1s Binding Energy Values and Atomic Charges Obtained from XPS and DFT Calculations[a]

nitrogen atom	experimental binding energy (eV)	calculated core energy (eV)	atomic charge[b]
[MAT]I			
N_{RA}	402.0	402.0	−0.04
N_{RM}	401.7	401.8	−0.04
N_R	400.1	400.4	−0.06
N_A	400.1	400.2	−0.16
Na[DCA]			
N_{DC}	399.6	399.6	−0.13
N_{DT1}	398.3	398.6	−0.19
N_{DT2}	398.3	398.6	−0.19
[MAT][DCA]			
N_{RM}	402.3	402.3	0.03
N_{RA}	402.1	402.2	0.03
N_R	400.5	400.4	−0.04
N_A	400.5	399.6	−0.14
N_{DC}	399.1	397.9	−0.14
N_{DT1}	397.9	396.9	−0.25
N_{DT2}	397.7	396.8	−0.27
[BMIM]Cl			
N_{RB}	401.2	401.2	−0.04
N_{RM}	401.2	401.2	−0.04
[BMIM][DCA]			
N_{RB}	401.6	401.6	0.01
N_{RM}	401.4	401.6	0.01
N_{DC}	399.2	398.2	−0.16
N_{DT1}	398.0	397.1	−0.28
N_{DT2}	397.8	397.0	−0.24

[a]N_{RM}: ring N bonded to methyl group; N_{RA}: ring N bonded to amino group; N_R: ring N, unsubstituted; N_A: amino N; N_{DC}: central [DCA]$^-$ N; N_{DT}: terminal [DCA]$^-$ N; N_{RB}: ring N bonded to butyl group. [b]Atomic charges were obtained using the Lowdin Population Analysis,[88] which is a Mulliken population analysis[89−91] based on symmetrically orthogonalized orbitals.

energies for each nitrogen center in the four systems. The agreement between theory and experiment is generally quite good and certainly good enough to assign the spectra unambiguously. The two highest binding energies (~402 eV) are assigned to the ring N atoms in [MAT]$^+$ that have methyl and amino substituents, N_{RM} and N_{RA}, respectively, while the

unsubstituted ring nitrogen (N_R) and amino group nitrogen (N_A) contribute to the lower binding energy peak (~400 eV). For [BMIM]$^+$, the two ring nitrogen atoms (methyl and butyl substituted, N_{RB} and N_{RM}) give overlapping contributions to a peak around 401.5 eV. For [DCA]$^-$, theory agrees with the assignment discussed previously, namely, that the central N atom (N_{DC}) has higher binding energy and the two terminal N atoms (N_{DT}) have lower binding energies. This assignment is consistent with the calculated atomic charges listed in Table 1, which predict the two terminal nitrogens to be more negatively charged ($-0.19e^-$) than the central nitrogen ($-0.13e^-$).

Note that for the ILs the calculated N 1s binding energies for the [DCA]$^-$ anion appear to be ~1 eV lower; however, this is misleading. In fact, what we can say is that the splitting between N 1s peaks associated with the cation versus the anion is about 1 eV larger. The fact that the discrepancy appears to affect only the anion is an artifact of using the highest binding peak (on the cation) to correct the theoretical values. This discrepancy suggests that the average chemical environment surrounding the various N atoms is different in a room-temperature IL compared to an isolated ion pair, reflecting both thermal deviations from the minimum energy structure and the presence of many additional ions in the surroundings. The observation that the splitting is smaller in the IL than in the ion pair suggests that, as expected, interactions with neighboring ions tend to reduce the cation−anion charge difference compared to an isolated ion pair.

C 1s high-resolution spectra (Figure 2) were also analyzed for the same set of samples; however, their interpretation is more challenging. The difficulty results partly from the presence of carbonaceous adsorbates which deposit on any sample exposed to laboratory atmosphere and partly because there is less structure in the C 1s spectra. A common practice used to identify and reduce the contribution of adventitious carbon in XPS is to take spectra before and after using high-energy Ar$^+$ ions to sputter away the surface layer of the sample. This process also damages molecules in the near-surface region probed by XPS, thus the results have to be interpreted with caution. Lovelock et al.[61] have shown that clean surfaces can be obtained by sputtering for the [C$_n$C$_1$Im][Tf$_2$N] IL systems. Data showing sputtering effects on the ILs and other materials of interest for the two IL systems studied here are presented in the SI. Unfortunately, some of the materials, particularly Na[DCA] and [BMIM]Cl, are rapidly and extensively damaged by Ar$^+$ sputtering, and for this reason most of the discussion focuses on the spectra of unsputtered samples. We note, however, that for the N 1s spectra, which provide the most insight into the IL structure and binding to the boron surfaces, the spectra of the ILs, themselves, are essentially unaffected by sputtering; i.e., the adventitious adsorbates have negligible effects. The major contribution from adventitious adsorbates is significant on the C 1s spectra, and for these spectra we used sputtering to identify the peaks arising from adventitious sources but did not attempt to completely remove the contaminants.

The data on sputtered surfaces show that adventitious carbon made its major contribution to a single peak in each spectrum, and as is common, we have used this adventitious carbon peak as a binding energy reference, shifting each spectrum to put adventitious C 1s at 284.5 eV.[48] This reference method works well in this system, giving binding energies for B^0 and B^{3+} that are in excellent agreement with literature values, as shown below.
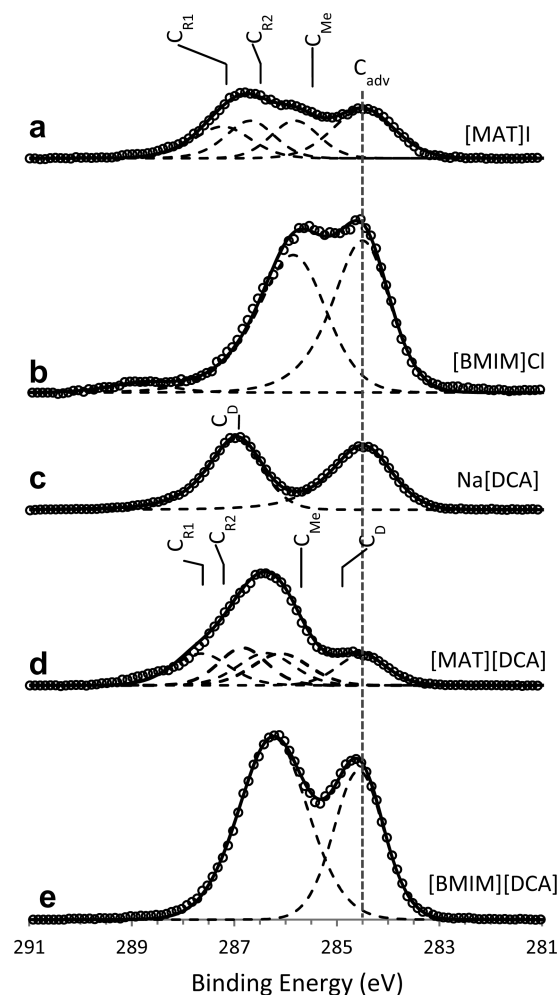

Figure 2. C 1s high-resolution XPS scan of (a) [MAT]I, (b) [BMIM]Cl, (c) Na[DCA], (d) [MAT][DCA], and (e) [BMIM]-[DCA].

The C 1s spectra in Figure 2 are for unsputtered [MAT]I, [BMIM]Cl, Na[DCA], [MAT][DCA], and [BMIM][DCA], with the adventitious C 1s peak indicated by a vertical dashed line. The C 1s binding energies from DFT calculations are shown as vertical lines above each spectrum, and the theoretical and experimental binding energies are summarized in Table 2. For the [MAT]$^+$-containing samples, assignments can be made by comparing DFT and experiment. The three carbon atoms in [MAT]I have calculated binding energy values ranging from 285.5 to 287.2 eV, with the ring carbons having higher energies than the methyl carbon. These three peaks overlap to form a single asymmetric feature, which can be seen more clearly when the adventitious signal is reduced by sputtering (SI Figure S6). The two carbon atoms of the Na[DCA] are identical, with a C 1s binding energy of 286.9 eV—surprisingly high considering that this is an anion. The DFT results are in good agreement with this observation, however, and explain the high binding energy by showing that the negative charge is delocalized on the three N atoms, with the C atoms having negligible charge.

Since the observed C 1s binding energies of [MAT]I and Na[DCA] are in the same range, it is not surprising that the spectrum for [MAT][DCA] consists of a single peak. The experiment suggests that the C 1s binding energy for the [DCA]$^-$ carbon atoms in the IL are shifted lower than in Na[DCA], and again this suggestion is consistent with the DFT

Table 2. C 1s Binding Energy Values and Atomic Charges Obtained from XPS and DFT Calculations[a]

nitrogen atom	experimental binding energy (eV)		calculated core energy (eV)	atomic charge[b]
[MAT]I				
C_{R1}	287.2		287.2	−0.11
C_{R2}	286.7		286.5	−0.04
C_{Me}	285.8		285.5	−0.13
Na[DCA]				
C_{D1}	286.9		286.7	−0.03
C_{D2}	286.9		286.7	−0.03
[MAT][DCA]				
C_{R1}	287.6		287.6	0
C_{R2}	286.8		287.2	−0.01
C_{Me}	286.4		285.7	−0.10
C_{D1}	286.3		284.9	−0.07
C_{D2}	286.2		284.8	−0.05
[BMIM]Cl				
C_{R1}	Peak 1		287.2	−0.08
C_{R2}			286.0	−0.09
C_{R3}			286.0	−0.09
C_{Me}			286.0	−0.13
C_{B1}			286.0	−0.10
C_{B2}	Peak 2		285.0	−0.18
C_{B3}			284.8	−0.17
C_{B4}			284.5	−0.23
[BMIM][DCA]				
C_{R1}	Peak 1		287.1	−0.03
C_{R2}			286.2	−0.05
C_{R3}			286.2	−0.07
C_{Me}			285.8	−0.11
C_{B1}			286.4	−0.08
C_{B2}	Peak 2		284.8	−0.17
C_{B3}			284.0	−0.18
C_{B4}			283.7	−0.23
C_{D1}			284.8	−0.09
C_{D2}			284.6	−0.09

[a]$C_{R1−R3}$: unsubstituted ring carbons; C_{Me}: methyl carbon; $C_{D1,D2}$: dicyanamide carbons; $C_{B1−B4}$: butyl carbons. [b]Atomic charges were obtained using the Lowdin Population Analysis,[88] which is a Mulliken population analysis[89−91] based on symmetrically orthogonalized orbitals.

results, although as discussed above, DFT gives the cation–anion splittings that are larger than in the experiment.

The experimental [BMIM]Cl and [BMIM][DCA] C 1s spectra show two relatively sharp peaks, one of which clearly is at least partly due to adventitious carbon. This adventitious carbon peak does not sputter away in [BMIM][DCA] to the same extent as in the other samples (SI Figure S4). This suggests that this peak may have contributions from the [BMIM]+ cation[57] based on the fact that this peak is also present in [BMIM]Cl. Figure 2e does not show individual experimental fit components because there is simply no unambiguous way to fit two peaks with more than eight distinguishable C 1s binding energies (eight from [BMIM]+, plus a pair from [DCA]−). The figure also does not indicate the DFT-estimated C 1s binding energies, simply for lack of space. The DFT results are given in Table 2 and are in good agreement with the observation that there are two groups of binding energies, one around 284.5 eV and one around 286 eV.

The sputtering results shown in the SI (Figures S1−S11) are peripheral to the main point of this study but are interesting enough to warrant a brief description. For [MAT]I, [MAT]-[DCA], and [BMIM][DCA], sputtering resulted in relatively minor changes in the C 1s and N 1s spectra, apart from the decrease in the C 1s peaks thus identified as arising from adventitious carbon. In particular, the peak positions shifted very little, and there are no major intensity changes. The changes are consistent with the sample remaining largely unchanged, with a small admixture of damaged molecules in the top few nanometers of the samples, probed by XPS.

In contrast, sputtering causes dramatic changes in the [BMIM]Cl and Na[DCA] samples, as shown by the C 1s and N 1s spectra (SI Figures S7−S11). For [BMIM]Cl, the N 1s signal dramatically broadened, and the integrated intensity decreased significantly, indicating preferential loss of nitrogen from sputtering. The C 1s signal shifted to higher binding energy with sputtering; the intensity in the range attributed to adventitious and aliphatic carbon signals was also reduced dramatically; and the total C 1s signal increased substantially, indicating an increase in the fraction of carbon in the near-surface region. Finally, there was a larger-than-normal increase in the background pressure during sputtering, suggesting substantial evolution of a gaseous product. The fact that the changes are so dramatic, affecting essentially all molecules in the near-surface region, suggests that sputtering triggers decomposition. There may also be some conversion of the Cl− to an alkyl chloride, as suggested by the observation that the Cl 2p peak (SI Figure S9) also shifted to a higher binding energy after sputtering, which is characteristic of such compounds.[62]

For Na[DCA], the N 1s spectrum also changes dramatically with a substantial decrease in N intensity, a shift of the main spectral features to lower binding energy, and growth of a small feature at ~404 eV, which is well above the range typically seen in oxygen-free organo-nitrogen compounds.[63] In contrast to the [BMIM]Cl results, where the C 1s spectrum shifts to higher binding energy, the Na[DCA] C 1s signal shifts to substantially lower binding energy with essentially no signal remaining at the unsputtered peak position. Again, these results suggest that sputtering initiates some decomposition chain reaction that destroys all the molecules in the near-surface region. While these observations have no effect on interpretation of the XPS results, they are interesting examples of severe sputter damage and can be compared to the thermal decomposition results discussed below.

B. Summary of Particle Properties. We previously[46] showed that boron milled with [MAT][DCA] generated particles mostly in the 50−70 nm size range, with a tail running out to ~150 nm. The particles were coated with a solvent-resistant IL layer that prevented oxidation upon exposure to air. The question of how an IL like [MAT][DCA] could bind strongly to boron surfaces prompted the present investigation into the binding mechanism. Given that boron is generally considered to be electron deficient,[64] one potential binding motif is complexation of the [MAT]+ cation to boron via interaction of the lone pair on the amino group; however, one might also expect that the anion might bind via lone pairs on either the central N atom or the nitrile groups. For comparison purposes, therefore, we also produced boron nanoparticles by milling with the IL [BMIM][DCA], which has the same anion but a cation without an amino substituent. Boron milled with [BMIM][DCA] produced a black viscous

suspension, which showed some sign of settling after 48 h, similar to that formed by milling with [MAT][DCA]. DLS measurements of the [BMIM][DCA]-coated nanoparticles dispersed in ethanol (Figure 3) showed a relatively sharp
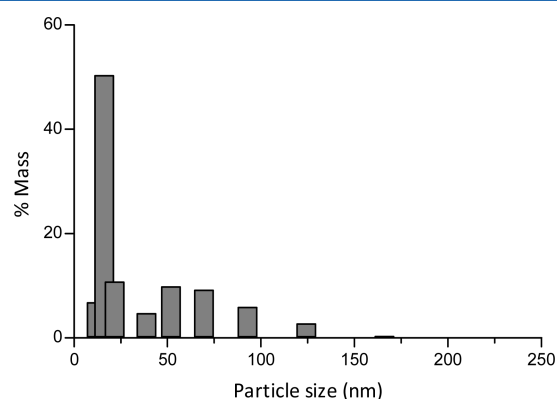
Figure 3. Mass weighted DLS size distribution of boron [BMIM]-[DCA].

feature around 20 nm in the mass-weighted size distribution, with a broad tail extending to ~125 nm, which may result from aggregates of smaller primary particles. This represents a significant shift to smaller particles, compared to those produced with [MAT][DCA] under identical conditions, possibly because [BMIM][DCA] is less viscous.[15,65] SEM imaging of samples washed with ethanol as described above showed individual irregularly shaped boron particles 50−70 nm in diameter; however, TEM (Figure 4) suggests that these large particles seen in SEM are aggregates formed in drying of primary particles that appear to be ≤20 nm. Electron energy loss spectroscopy (EELS) analysis confirmed that the particles observed are indeed composed of boron with traces of nitrogen, carbon, and oxygen, which presumably reflect some contribution from the IL and from adventitious adsorbates.

Trace amounts of tungsten and cobalt contaminants originating from the milling media and jar were observed in XPS (SI Figure S14). We previously demonstrated that this contamination is in the form of small particles and that the contamination level can be reduced substantially by simply stirring the milling products with a magnetic stir bar, which collects the cobalt-cemented tungsten carbide particles quite efficiently.[45]

We also produced particles by milling boron with the salts [MAT]I, [BMIM]Cl, and Na[DCA], which contain only one of the cations or anions that make up the two ILs of interest. Because our interest in the salt-milled particles was in their surface chemistry, we did not characterize size distributions or other particle properties.

C. Boron Nanoparticle Passivation by ILs. The oxidation state of boron nanoparticles milled under different conditions was studied using XPS, taking advantage of the low IL vapor pressures[56,66] to study both washed and IL-wetted particles. For unoxidized elemental boron (B^0), the B 1s binding energy is 188 eV, and when fully oxidized to B_2O_3 (B^{3+}), the B 1s binding energy is shifted by 5 to 193 eV.[48] As shown in Figure 5a, when boron nanoparticles are produced, as described above, but with no passivating agent (only acetonitrile to prevent caking of the dry powder), then air-dried prior to transfer to the XPS instrument, peaks are observed for both elemental boron in the core of the particles and B^{3+} in the oxide layer that
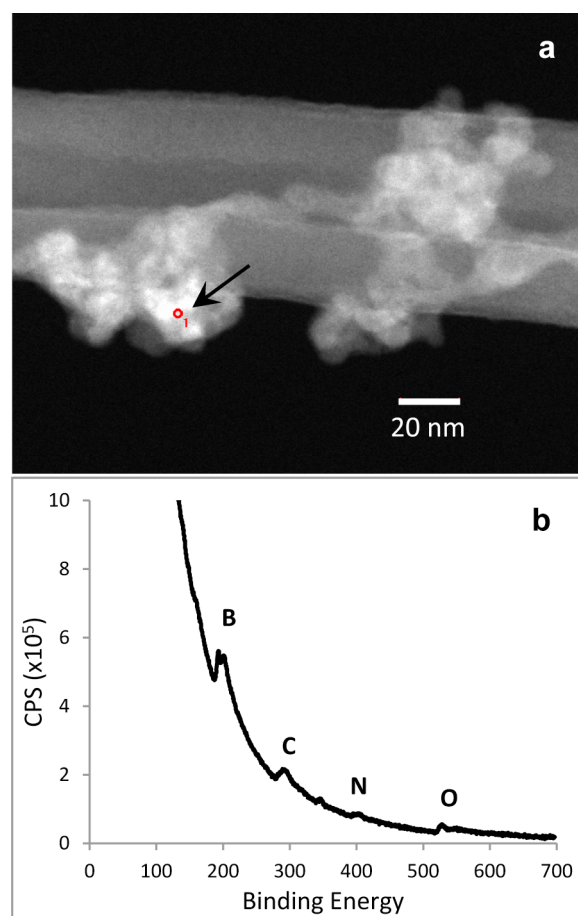

Figure 4. (a) High-resolution TEM image of boron nanoparticles. (b) EELS spectrum of the area marked with a circle on image (a).

spontaneously formed upon air exposure. As discussed previously, the intensity of the B^{3+} peak for milled, unpassivated boron is actually substantially larger than it is for unmilled, oxidized boron.[45] This effect is attributed to the deposition of dissolved boron oxide or small, completely oxidized boron particles, on the surface of the sample when it is dried for analysis.

When boron is produced in either [MAT][DCA] or [BMIM][DCA], and the IL-wetted nanoparticles are analyzed without washing (Figures 5b and e), no signal is observed for either elemental boron or fully oxidized boron. Instead, there is a weak signal (note scale factors in the figure) for boron with B 1s binding energy of ~191.5 eV, corresponding to some intermediate oxidation state (B^{n+}). If the particles are thoroughly washed with ethanol, as described above, to remove excess IL (Figures 5c and f), then XPS shows a substantial peak for B^0, with a weak tail that extends into the region corresponding to B^{n+} and little if any signal for fully oxidized B^{3+} at 193 eV. Finally, if the ethanol used in the washing process is evaporated to recover the excess IL washed off of the particles, XPS of this residue shows a small amount of boron, predominantly corresponding to the intermediate oxidation state, B^{n+} (Figure 5d and g). Note that an alternative explanation for the 191.5 eV feature in the B 1s spectra of milled samples might be the formation of some boron particles that are so small that charging and screening of the photoemission core hole state is inefficient compared to bulk boron, resulting in higher measured B 1s binding energy. The
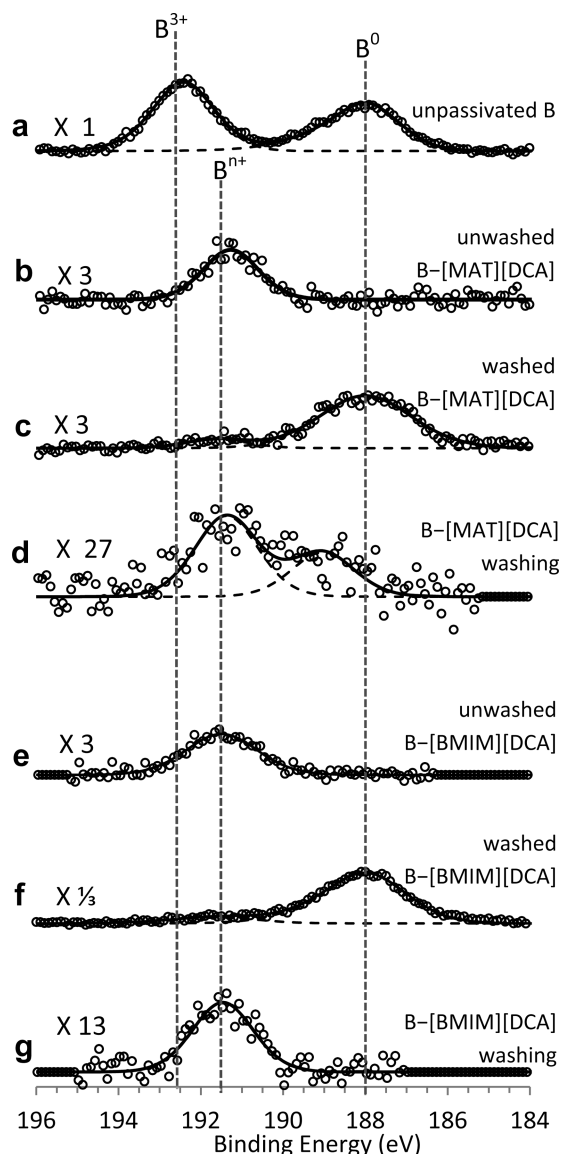
Figure 5. B 1s high-resolution XPS scan of (a) boron milled with acetonitrile with no added IL, (b) boron milled with [MAT][DCA] unwashed, (c) boron milled with [MAT][DCA] completely washed with ethanol, (d) [MAT][DCA] recovered from a milled boron sample after washing with ethanol, (e) boron milled with [BMIM]-[DCA] unwashed, (f) boron milled with [BMIM][DCA] completely washed with ethanol, and (g) [BMIM][DCA] recovered from the milled boron sample after washing with ethanol.

presence of substantial N 1s XPS signals is consistent with the presence of a capping layer derived from the ILs.

Comparison of the B 1s intensities of the B^0 peak in the washed samples (Figure 5c and f—note scale factors) shows that the B 1s signal from boron coated with [MAT][DCA] is ~10 times smaller than the signal observed from particles coated with [BMIM][DCA]. Given that the particles in each case are solid boron, the variations in intensity indicate that the solvent-resistant capping layer is substantially thicker (resulting in more attenuation of electrons from the underlying boron) for boron milled with [MAT][DCA] than for boron milled with [BMIM][DCA]. This conclusion is supported by the observation that the N 1s intensity is ~3 times greater for boron capped with [MAT][DCA] than for boron capped with [BMIM][DCA] (SI Figure S14), whereas the ratio of the number of N atoms is only 7:5 in the two ILs. As discussed in the SI, the intensities in Figure 5 can be used to estimate that the [MAT][DCA] capping layer is ~2 nm thicker than that for [BMIM][DCA]. TGA and IR results below provide additional insight into this issue, and the estimates of the layer thicknesses are given below.

The fact that neither B^0 nor B^{3+} signal is observed for the unwashed samples simply means that the boron particles are buried under a thick enough layer of IL that blocks detection of electrons emitted from the particles. As mentioned above, the effective attenuation length for B 1s photoelectrons in a material with the composition and density of these ILs is calculated to be ~3.3 nm,[67] thus the particles are invisible to XPS unless they are within ~10 nm of the liquid surface. Instead, the XPS signal is observed from some intermediate oxidation state boron (B^{n+}) that is dissolved or suspended in the IL, such that it has significant concentration in the top 10 nm of the IL. The presence of this B^{n+} boron in the ILs recovered from washing confirms this conclusion. The B^{n+} binding energy of ~191.5 eV observed for this dissolved/suspended boron could correspond to a suboxide; however, we note that the B 1s binding energy for boron nitride is reported to be in this range,[68] and while we do not suggest that boron nitride is formed in the milling process, it may be that this feature represents boron atoms or small boron clusters bound to the N-rich ILs, or some B_xN_y compound formed under our milling conditions, which is soluble in the ILs. We note that the ILs recovered from the washings are slightly darker in color than the IL starting materials.

One interesting question is whether the local high temperatures and mechanical forces generated during milling are required for formation of an effective passivating IL layer or if it is sufficient to simply allow clean boron surfaces to interact with neat ILs, after completion of the milling process. This question was tested for both [MAT][DCA] and [BMIM][DCA] by milling boron with only acetonitrile as a dispersing agent and then ultrasonicating the resulting boron particles with one or the other IL. These "post-milling IL-capping" experiments are described in more detail, and the data are presented in the SI (Figures S12 and S13). In brief, it was shown that a capping layer is formed by ultrasonicating boron with either of the ILs, that this capping layer persists after ethanol washing, and that it largely protects the boron from oxidation during subsequent air exposure. Comparison of Figures 5 and S12 (SI) shows, however, that protection against oxidation is significantly better for the particles milled with the ILs, compared to the particles that were ultrasonicated with the ILs after milling. It is possible that the milling really does drive more complete reaction of

fact that this 191.5 eV peak is diminished in the washed samples might simply indicate that such small particles tend to be lost in the washing/centrifuging process used to remove the excess IL from the particles.

Comparison of the XPS for washed particles (Figures 5c and f) with that for unpassivated boron (Figure 5a) shows that the washed particles must still be coated with a dense enough layer of IL to passivate the boron so that it does not oxidize during air exposure (for >8 h). This IL layer is bound strongly enough to resist removal by repeated ultrasonication in ethanol, which is a good solvent for the ILs. Acetonitrile is a better solvent for these ILs; however, we avoided the use of any N-containing solvents to eliminate N 1s contributions from the solvent in the XPS. As shown in the survey spectra in SI Figure S14, the

boron with the ILs, resulting in a better capping layer; however, we note that in the "post-milling IL-capping" experiments the particles have substantial exposure to the glovebox atmosphere during the postmilling workup, while the particles milled with ILs are capped immediately as they form. They, therefore, would be much less affected by possible oxidation by contaminants in the glovebox atmosphere.

D. Boron Nanoparticle–IL Interaction. Imidazolium-based ILs have been previously used as stabilizing agents in the synthesis of metal nanoparticles,[59,69−74] but not for highly reactive materials like boron. Calculations[70,75] and empirical[69] data suggest a number of possible motifs for interaction of these ILs with nanoparticles. Surface-enhanced Raman spectroscopy (SERS) studies done by Dupont's group on imidazolium IL-stabilized gold nanoparticles suggest a strong interaction between the imidazolium cation and the gold nanoparticle surface through a parallel coordination, where the imidazolium ring lies flat on the gold surface while a long chain ether functional group is directed away from the surface, providing steric stabilization.[74] Zhang et al. arrived at a similar conclusion using XPS to study imidazolium-functionalized gold and platinum nanoparticles. In addition, they found that reactive substituents (i.e., R−COOH, R−NH$_2$) on the imidazolium ring provided an alternative interaction with the nanoparticles.[59] Other evidence regarding imidazolium−metal interactions was obtained from ^{2}H NMR studies of functionalized iridium nanoparticles, which suggested formation of an N-heterocyclic carbene.[73] In addition to these studies suggesting that IL−metal interactions are dominated by the cation, there is work documenting the role of the anion. Anions with strongly coordinating atoms like F and O (i.e., BF$_4^-$, PF$_6^-$, and CF$_3$SO$_3^-$) were found to interact strongly with iridium nanoparticles, forming nonstoichiometric cationic and anionic supramolecular aggregates on the surface.[72] Khare also concluded that stabilization of Fe$_3$C nanoparticles with dicyanamide- and thiocyanate-containing ILs was due to the complex formed by either anion with iron.[71] For a material like boron, which is considered to be electron deficient, hence highly reactive, readily forming stable hydrides, carbides, oxides, and nitrides, it is not at all clear what interactions might be expected for ILs like [BMIM][DCA] or [MAT][DCA].

We probed the IL−boron interactions using a combination of XPS, FTIR, TGA, and zeta potential measurements. N and C 1s XPS analyses were performed on the same ethanol-washed boron nanoparticle samples used for the B 1s spectra in Figure 5c and f. Figure 6 compares the N 1s spectra of the IL-covered boron nanoparticles with the spectra of the corresponding pure ILs. In both cases, the highly structured N 1s spectra seen for the pure ILs collapsed into broad and almost featureless peaks for nitrogen in the IL capping layer. In particular, the higher binding energy peaks associated with the [MAT]$^+$ or [BMIM]$^+$ cations are substantially weakened in the IL−boron spectra, with the corresponding intensity shifted to lower binding energy. The residual intensity at high binding energies may, in fact, simply result from a small amount of free IL that was not washed from the sample by our three-step sonication−centrifugation process. In [MAT][DCA]−boron, the peaks associated with free [DCA]$^−$ shifted to higher binding energy, so that all the N 1s signal collapses into a single, relatively compact feature at intermediate binding energies. Core level binding energies shift depending on the charge on the atoms emitting the electrons, as exemplified by the splitting between N 1s peaks from the cations and anions of the free ILs. The fact
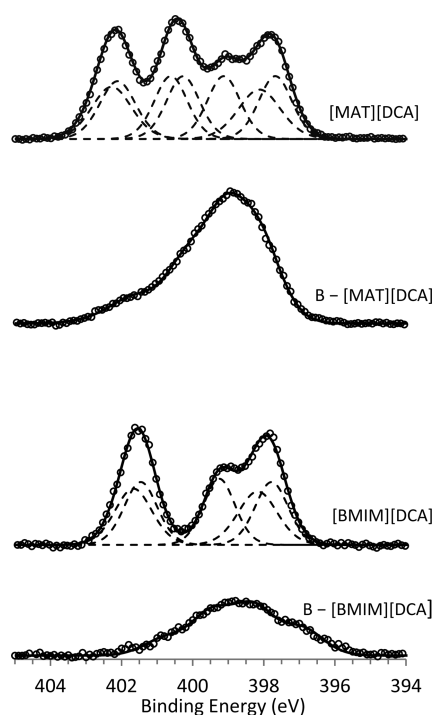

Figure 6. N 1s high-resolution scan of [MAT][DCA], boron milled with [MAT][DCA], [BMIM][DCA], and boron milled with [BMIM][DCA].

that the N atoms in the [MAT][DCA]−boron sample all have similar 1s binding energies suggests that the charge distribution in the capping layer is no longer strongly polarized. For [BMIM][DCA]−boron, a similar merging of cation- and anion-derived peaks into a single feature occurs, although the resulting feature is broader. The lower intensity observed for [BMIM][DCA]−boron is additional evidence that the capping layer is thinner for [BMIM][DCA]−boron than for [MAT][DCA]−boron.

C 1s spectra of the IL-coated boron samples are given in the SI (Figure S15). Because there was less structure in the carbon spectra of the pure ILs, it is harder to infer anything about binding from the boron−IL spectra. For [MAT][DCA]−boron, where the pure IL spectrum only has a single broad peak, the spectrum shows a slight shift and broadening toward higher binding energies. For [BMIM][DCA]−boron, where the pure IL showed two peaks, the spectrum collapses to a single, broad, almost structureless feature.

To help understand the IL−boron interaction, we also measured XPS of samples prepared by milling boron with [MAT]I, [BMIM]Cl, and Na[DCA]. Since these reagents are solids at room temperature, ethanol was added to the milling mix to avoid caking and achieve efficient mixing during milling. All three salts are quite soluble in ethanol, which was used to avoid introducing any other source of nitrogen. Prior to XPS analysis, samples were washed thoroughly with ethanol, as described above, to remove any material that was not bound tightly to the boron particles. Figure 7 shows the N 1s spectra of boron milled with [MAT]I, [BMIM]Cl, and Na[DCA]. Note that the sample prepared with [MAT]I and then washed still has significant N 1s intensity, indicating that [MAT]I is bound to the surface strongly enough to resist removal by repeated ultrasonic washing. In addition to the two peaks at 400 and 402 eV, characteristic of [MAT]$^+$ in pure [MAT]I and
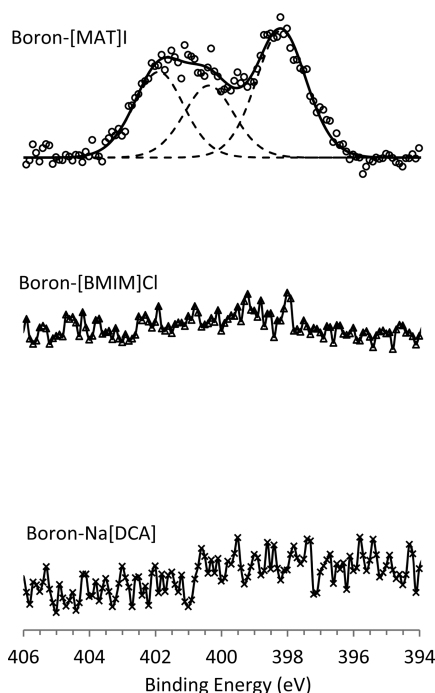
Figure 7. N 1s high-resolution XPS scan of boron samples milled with [MAT]I, [BMIM]Cl, and Na[DCA].

[MAT][DCA] (Figure 1), there is a new peak at ∼398 eV, which is the N 1s binding energy for nitrogen in boron nitride[76] and which we attribute to formation of B−N bonds between [MAT]$^+$ and boron. The presence of all three peaks tends to suggest that the capping layer for boron−[MAT]I contains roughly equal amounts of [MAT]$^+$ that still looks like the free cation and [MAT]$^+$ that has reacted with the boron surface. In contrast, boron milled with [BMIM]Cl or Na[DCA] and washed shows essentially no XPS signal in the N 1s region, indicating that [BMIM]Cl and Na[DCA] were completely washed out of the sample.

It is tempting to interpret these results as showing that the [MAT]$^+$ cation binds to boron surfaces, while both [DCA]$^-$ and [BMIM]$^+$ do not; however, several observations indicate that the situation is more complex and that binding depends on both the cation and anion and interactions between the two. For example, while [BMIM]$^+$ and [DCA]$^-$ do not bind strongly to boron when paired with Cl$^-$ and Na$^+$, respectively, the [BMIM][DCA] combination does form a dense, solvent-resistant capping layer. It is also interesting that while the N 1s spectrum of boron−[MAT]I shows signs of both free [MAT]$^+$ and nitrogen making strong B−N bonds, there is essentially no signature for free [MAT]$^+$ in the capping layer formed for boron−[MAT][DCA], despite the indications from B 1s XPS and TGA (see below) that the capping layer for boron−[MAT][DCA] is relatively thick. The fact that the anion is [DCA]$^-$ in one case and I$^-$ in the other may affect both boron−[MAT]$^+$ binding, hydrogen bonding within the capping layer, and the extent to which charge is redistributed between cation and anion. For example, I$^-$ and [DCA]$^-$ are quite different in size and shape, and the electron affinity of the [DCA]$^-$ radical has been measured to be 4.14 eV[77] compared to 3.06 eV[78] for iodine atoms. It could be that I$^-$ tends to bind to the boron surface to some extent, helping to stabilize the [MAT]I capping layer, and that [BMIM]Cl and Na[DCA] do

not form a solvent-resistant layer partly because the Cl$^-$ and Na$^+$ counterions do not interact with boron strongly enough.

In the case of the [BMIM]$^+$ cation, although it has been found that metal nanoparticles may interact with the imidazolium ring lying flat on the surface,[74] this interaction may not be strong enough to prevent it from being removed from the boron surface through rigorous ultrasonic washing by ethanol. Data from zeta potential experiments presented later confirmed this conclusion.

Infrared spectroscopy provides additional insight into the binding of the ILs to boron surfaces. Figure 8 compares spectra
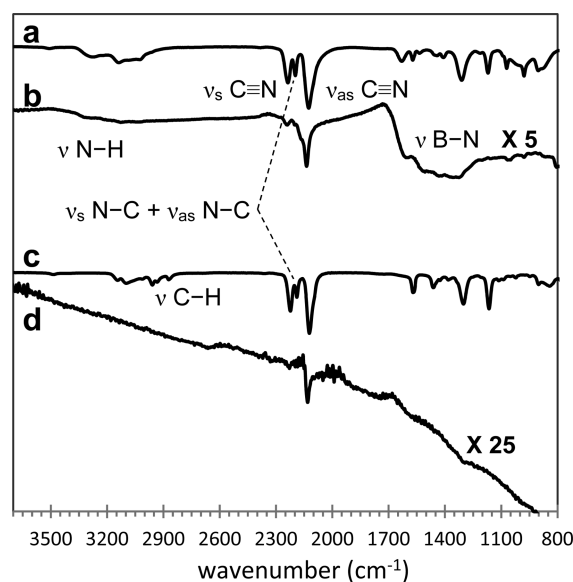

Figure 8. FTIR spectra of (a) neat [MAT][DCA], (b) boron milled with [MAT][DCA] washed with ethanol, (c) neat [BMIM][DCA], and (d) boron milled with [BMIM][DCA].

of neat [MAT][DCA] and [BMIM][DCA] with those for ethanol-washed samples of boron capped with each IL. One obvious point is that the signatures of IL binding in the [BMIM][DCA] case are substantially weaker than those for [MAT][DCA] (note scale factors), providing additional evidence that the capping layer is thicker in the latter case. The strongest spectral feature for both ILs is a group of three intense peaks at 2246, 2193, and 2126 cm^{-1} which have been assigned as vibrations of [DCA]$^-$.[79] These are, respectively, the symmetric C≡N stretch (ν_s), overlapping symmetric and asymmetric stretches of the N−C bonds about the central N (ν_{as} N−C + ν_s N−C), and the asymmetric C≡N stretch (ν_{as}). In addition, N−H and C−H stretches from the amino and methyl groups, respectively, were also observed in the 3300−3000 cm^{-1} region[79] for [MAT][DCA], while the C−H stretching modes from the methyl and butyl substituents were observed from 2980 to 2900 cm^{-1} for [BMIM][DCA].

For the ILs on boron, all the IL-specific peaks decrease substantially in intensity (note scale factors), presumably because the IL capping layers are thin compared to the IL layer studied for the neat ILs. The N−H stretch in [MAT][DCA] appears to be broadened and shifted to higher wavenumbers for boron−[MAT][DCA], and the various C−H stretches for both ILs are nearly absent in the boron−IL samples. The effect on the N−H stretch would be consistent with binding of [MAT]$^+$ to the surface via interaction of the amino group. Also, B−N bond formation is consistent with the

appearance of a broad peak at about 1350 cm^{-1} that has been attributed to a B—N stretching mode.[80,81] The absence of such a feature for [BMIM][DCA], which has no amino group, would be consistent with this scenario.

Note, however, that the spectral features associated with [DCA]$^-$ are also strongly perturbed by binding to the surface, suggesting that the anion is also involved in the binding. In particular, the symmetric C≡N stretch and C—N stretching bands are attenuated substantially compared to the asymmetric C≡N stretching bands in both [MAT][DCA] and [BMIM]- [DCA] samples. These changes in features associated with [DCA]$^-$ suggest that there must also be boron−[DCA] interactions, as have been seen for titanium nanoparticles.[82] If, for example, one of the terminal N atoms in [DCA]$^-$ reacted with boron, this would break symmetry, eliminating both symmetric stretch modes and leaving a single C≡N stretch of the nonbonded end of the DCA. Both the XPS and IR results, therefore, tend to suggest that there is strong boron−[MAT]$^+$ bonding, likely involving the amino group. However, there appears to be interaction of [BMIM]$^+$ and [DCA]$^-$ with the boron as well and that some degree of cooperativity between cation and anion binding to boron probably affects all these systems.

Another way of examining how ILs and salts bind to nanoparticle surfaces is by measuring the zeta potential of the samples. In essence, this technique applies an AC electric field across a sample of nanoparticles suspended in a solvent and measures the amplitude and direction of the resulting AC motion. The zeta potential is related to the electric potential at the boundary between the layer of ions that is attached to the particle surface tightly enough to move with it (the Stern layer), as opposed to the diffuse layer of counterions dissolved in the solvent.[83] Zeta potential is sensitive to the net charge of the ionic species binding on the particle surface. Figure 9 gives the zeta potentials measured for boron nanoparticles produced under a variety of conditions, using acetonitrile as an aprotic solvent. Using acetonitrile as an inert solvent eliminates the effect of pH changes, thus the measured zeta potentials are comparable to results obtained under neutral conditions. This was confirmed by measuring the zeta potentials of SiO$_2$ and
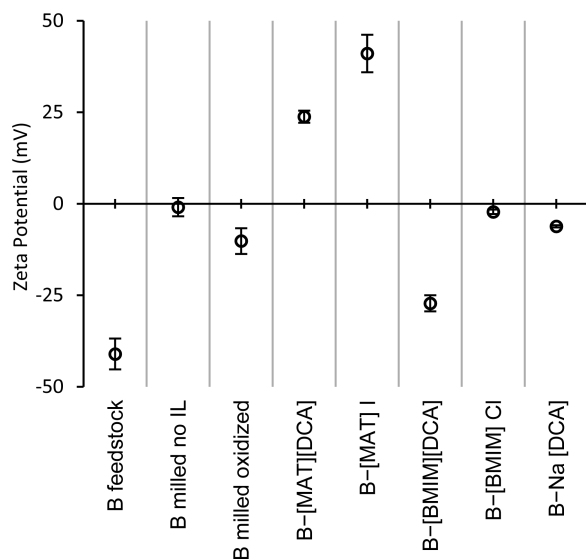
Al$_2$O$_3$ powder dispersed in acetonitrile, where both oxides displayed similar values to what is found for dispersions in water at pH 7.[84]

The unmilled boron feedstock has a zeta potential of about −42 mV, implying net anionic charging. The negative zeta potential presumably reflects the fact that the boron feedstock is covered by an oxide layer and probably has a significant coverage of adsorbed atmospheric water. When dispersed in a polar solvent, adsorbed water may hydrolyze leaving OH$^-$ species on the surface of the particle.

Boron milled in acetonitrile with no capping ligands and measured without exposure to O$_2$ beyond what could diffuse through the acetonitrile solvent resulted in a zeta potential of essentially zero (−1.0 ± 2.5 mV), probably because the oxide was dispersed in the acetonitrile, leaving an essentially neutral surface as the particles are crushed during milling. When the same boron particles were air-dried to allow oxidation, then resuspended in acetonitrile, the zeta potential (−10.2 ± 3.5 mV) was found to be intermediate between those of the oxidized feedstock and the milled unoxidized boron, confirming that boron surface oxidation tends to give a negative zeta potential.

When boron was milled with [MAT][DCA] and [MAT]I, the particles have positive zeta potentials, indicating that the strongly bound layer is dominated by the [MAT]$^+$ cation. In contrast, boron particles functionalized with [BMIM][DCA] showed a negative zeta potential, suggesting that in that system the strongly bound layer is dominated by [DCA]$^-$. Interestingly, the zeta potentials of boron milled with either Na[DCA] or [BMIM]Cl are essentially zero, which could mean either that the strongly bound layer has equal numbers of cations and anions or simply that neither of these salts binds significantly. The XPS results (Figure 7), which show almost no nitrogen on the surface of ethanol-washed samples of boron milled with Na[DCA] or [BMIM]Cl, demonstrate that these salts simply do not bind.

The zeta potential measurements reinforce the XPS finding that [MAT][DCA], [BMIM][DCA], and [MAT]I form solvent-resistant layers on boron surfaces and reveal whether these layers are dominated by anions or cations. Furthermore, the fact that the zeta potential for boron−[MAT]I is much more positive (+41 ± 5 mV) than that for boron− [MAT][DCA] (+24 ± 2 mV) suggests that in the latter case there is more anion binding, partially canceling the potential from the cations. The fact that the zeta potential for boron− [BMIM][DCA] is strongly negative indicates that the ionic surface layer is dominated by [DCA]$^-$ in this case, suggesting weak binding by [BMIM]$^+$, presumably because it lacks the amino group that seems to be involved in boron−[MAT]$^+$ binding. We propose that both cations and anions are interacting with boron in both cases; however, for [MAT]- [DCA] the stronger cation binding via the amino group gives a net positive charge, while for boron−[BMIM][DCA], the net negative charge indicates that the anion binding density is higher than that of the cation. Note that for [MAT][DCA] our results cannot distinguish clearly between dative B−N binding (B−N(H$_2$)−) and covalent BN binding, which would be accompanied by loss of one or more of the amino H atoms (either as H$_2$ or by formation of the B−H bond).

E. IL Desorption and Boron Nanoparticle Oxidation. As a final probe of IL−boron coordination, we used thermogravimetric analysis (TGA) to examine the thermal stability of the IL layer. One of the main motivations for coating

Figure 9. Zeta potential measurements of boron nanoparticles coated with ILs and other test ligands.

boron particles with ILs is to prevent oxide layer formation in ambient air, but of course it is important that oxidation occurs efficiently at higher temperatures, to allow boron ignition. Therefore, we studied the thermal behavior of pure [MAT]-[DCA] and [BMIM][DCA] and of boron nanoparticles capped with each IL in oxygen. The percentage mass change is plotted against temperature in Figure 10a. For the pure ILs, mass losses
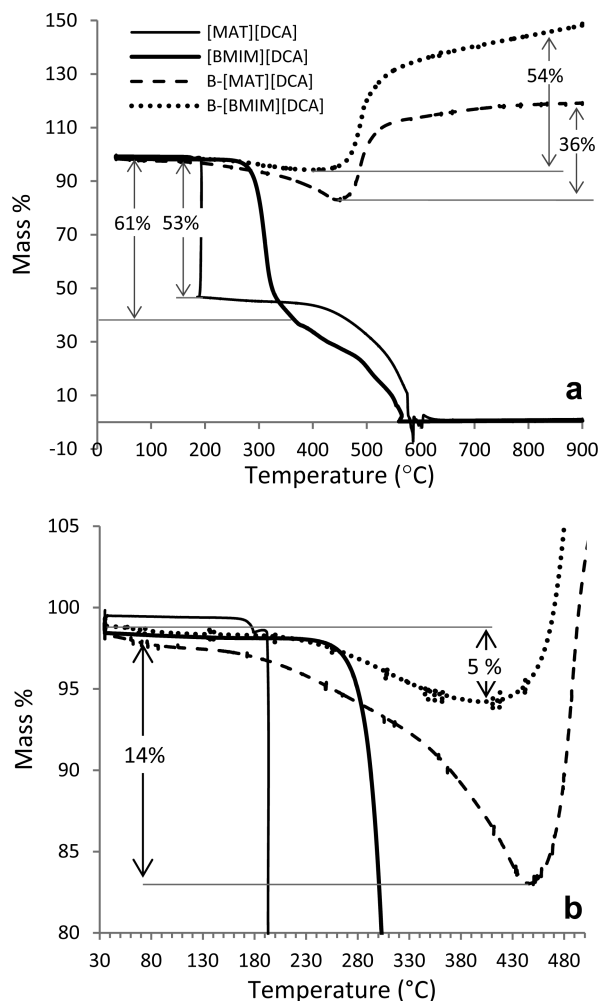

Figure 10. (a) TGA spectra of the neat ILs and boron samples milled with them. (b) Magnified portion showing mass decrease of boron-milled samples.

are expected, as the IL decomposes and/or is oxidized to gaseous products. For IL-capped boron, there should be mass loss associated with loss of the IL layer, but there is an offsetting mass gain associated with oxidizing the boron particle. Therefore, the net mass change for IL-capped boron will depend on the mass fraction of IL in the original samples.

For both ILs, two stage mass losses were observed, with the final mass near zero, indicating complete decomposition/combustion. For [MAT][DCA], the first stage is a sudden, isothermal mass loss of 53% at 192 °C, followed by a gradual decomposition/combustion leading to loss of the remaining mass over the temperature range from 370 to 580 °C. The residual mass at high temperatures is ∼0.84% of the initial mass. The initial 53% mass loss at 192 °C is comparable to the stoichiometric mass percentage of the [MAT]$^+$ cation (59.8%). Furthermore, TGA of [MAT]I under similar conditions shows

the onset of mass loss at about the same temperature, as shown in SI Figure S17. The similarity of these two measurements, together with the observation that the initial decomposition of [BMIM][DCA] occurs at much higher temperatures, indicates that this initial decomposition is triggered by the decomposition of the [MAT]$^+$. The material remaining after [MAT]$^+$ decomposition (probably a neutral derivative of [DCA]$^-$) may form polymeric products[85,86] before it is totally decomposed/oxidized in the temperature range between ∼400 and 580 °C. It is interesting that for [MAT]I >90% of the total mass is lost in the initial decomposition event, suggesting that [MAT]$^+$ decomposition leaves behind mostly products that are volatile at these temperatures. For example, it may be that in the decomposition process charge transfer results in formation of I atoms that recombine and desorb as I$_2$.

The TGA of [BMIM][DCA] shows initial decomposition starting at higher temperature (∼280 °C) and not quite as sharp as that for [MAT]$^+$ decomposition. The mass fraction lost initially is ∼61%, which is reasonably consistent with the mechanism being decomposition of the [BMIM]$^+$ cation (67% mass) to gaseous products. Furthermore, TGA analysis of [BMIM]Cl under the same conditions (SI Figure S18) shows essentially 100% mass loss at slightly lower temperatures, again suggesting that for the IL cation decomposition leaves material that must be slowly oxidized away, while decomposition of the cation in the salt leaves a volatile product, such as Cl$_2$ or some organic chloride. Interestingly, for [BMIM][DCA], the second stage of decomposition begins to occur at a temperature lower than for [MAT][DCA], although the decomposition/oxidation goes to completion at about the same temperature.

As the IL makes up only a fraction of the initial mass in the IL-capped boron samples and because mass gain from boron oxidation offsets mass loss from IL decomposition, oxidation of these samples is more complex. Figure 10b shows the same TGA results magnified to allow the subtle changes to be seen more clearly. For [BMIM][DCA]-capped boron, there is ∼5% mass loss in the range between 200 and 430 °C, by which point the pure [BMIM][DCA] IL would have lost >70% of its mass. (Note: The <1% mass losses seen below 200 °C probably just result from evaporation of residual ethanol that was used to wash excess IL from the particles, despite the fact that the washed particles were dried for more than 24 h at room temperature.) Starting around 430 °C, there is a rapid mass gain, and the 54% magnitude indicates that more than just a surface layer is oxidized; i.e., diffusion of oxygen and boron in the surface oxide layer that forms on the particles is fast enough to allow oxidation of the particle bulk. In this context, it is interesting to note that the melting point of bulk boron oxide is 450 °C,[87] thus significant bulk oxidation appears to require temperatures very close to the oxide melting point.

Several different limiting analyses of the mass loss/gain pattern are given in the SI, and the results are summarized here. One limiting analysis approach is to assume that all the IL leaves the surface as it is heated to ∼430 °C but that the boron surface does not oxidize at all in this temperature range. This assumption is not realistic, but it gives a rigorous lower limit on the amount of IL that could initially have been present on the particles. We also analyzed a variation on this scenario, where boron did not oxidize and the IL on the surface was assumed to have a mass loss identical to that in the neat IL (i.e., only a fraction of the IL is lost below 430 °C). A more realistic assumption is that the boron surface oxidizes to form a self-limiting oxide layer as the IL leaves the surface when the sample

is heated to 430 °C. We further assume that the fraction of IL that decomposes up to this temperature is the same on the boron surface as in the neat IL. Given that bulk oxidation does not occur below 430 °C, this set of assumptions results in an upper limit on the amount of IL that could have been present initially.

Table 3 lists the lower (column 1) and upper (column 3) limits on the mass of IL/nm^2 and the corresponding number of

Table 3. IL Coverage on Boron Nanoparticle Calculated TGA Data[a]

ionic liquid	1st scenario (B does not oxidize until IL is fully decomposed)		2nd scenario (B simultaneously oxidizes while IL decomposes)
	case 1	case 2	case 2
[MAT][DCA]			
mass density (fg/nm^2)	3.8×10^{-6}	7.1×10^{-6}	7.8×10^{-6}
ion pair density (IL/nm^2)	13.9	25.9	28.4
number of monolayers			
parallel to surface	5.8	10.9	11.9
perpendicular to surface	1.6	3.1	3.38
[BMIM][DCA]			
mass density (fg/nm^2)	6.2×10^{-7}	9×10^{-7}	1.6×10^{-6}
ion pair density (IL/nm^2)	1.8	2.6	4.7
number of monolayers			
parallel to surface	1.3	1.8	3.2
perpendicular to surface	0.2	0.3	0.6

[a]Case 1: mass loss is due to 100% decomposition of IL at 450 °C. Case 2: mass loss is due to partial decomposition of IL at 450 °C.

ion pairs/nm^2 present on the ethanol-washed particles. The table also gives estimates of how these limits correspond to the number of monolayers of IL, depending on whether the ILs lie parallel or perpendicular to the surface of the particle. For the [BMIM][DCA] capping layer, the lower and upper limits on the number of ion pairs/nm^2 are 1.8 and 4.7, and we expect that the true value should be closer to the upper limit. This upper limit corresponds to only ∼3 monolayers of IL bound to the surface, indicating that a quite thin IL layer is sufficient to block oxidation of the boron by air.

For [MAT][DCA], significant mass loss starts below the temperature where pure [MAT][DCA] begins to decompose, which may simply indicate that [MAT][DCA]-capped boron tends to retain ethanol (resulting in larger solvent mass loss) or could imply that the boron surface actually initiates [MAT]$^+$ decomposition at lower temperature. The initial mass loss rate is much less abrupt than that for pure [MAT][DCA], increasing slowly with temperature until mass gain suddenly becomes apparent between ∼430 and 450 °C (Figure 10b). The total mass loss to the minimum is 14%, and the mass gain relative to the minimum is only 36%.

Several points seem clear regarding the interpretation of the [MAT][DCA]-capped boron results. The larger mass loss indicates that the thickness of the solvent-resistant IL capping layer is substantially greater for [MAT][DCA] than for

[BMIM][DCA], consistent with the conclusions drawn from the XPS and IR data. Using the same assumptions discussed, the results in Table 3 are obtained. Note that the IL mass/nm^2 and number of ion pairs/nm^2 are substantially greater for [MAT][DCA] than [BMIM][DCA], consistent with the conclusions from XPS and IR. However, it is probably not reasonable to simply compare upper or lower limits for the two IL systems. For [BMIM][DCA], the IL layer is quite thin, thus it seems likely that boron oxidation should start quite early as the IL layer is removed, but for the much thicker [MAT]-[DCA] layer, it may be that there is not much boron oxidation over most of the temperature range below 430 °C. Nonetheless, if we compare the lower limit estimate for [MAT][DCA] with the upper limit for [BMIM][DCA], it is clear that the [MAT][DCA] layer is at least ∼3 times thicker than that for [BMIM][DCA], which is in reasonable agreement with the difference in the N 1s XPS signal for the two samples. Also, with the results obtained from B 1s XPS intensities that the [MAT][DCA] overlayer is ∼2 nm thicker than [BMIM]-[DCA], we can approximate a thickness of 3 nm for [MAT][DCA] and 1 nm for [BMIM][DCA], which is a reasonable estimate for a monolayer of [BMIM][DCA] and 2−4 monolayers of [MAT][DCA] oriented perpendicular to the surface of the nanoparticles (Table 3).

It is interesting that such a thick layer remains for [MAT][DCA] after our aggressive ultrasonic washing process. The data presented in Figure 10 for the B−[MAT][DCA] sample were already washed for a total of five times (two more than our typical three-cycle washing), but still a significant amount of [MAT][DCA] was observed. Another sample, washed ultrasonically for three cycles, gave a mass loss of 32% (i.e., 17% more than the five-times-washed sample in Figure 10). The observation that thick [MAT][DCA] capping layers survive such aggressive washing suggests that there are stronger cohesive interactions within the [MAT][DCA] compared to [BMIM][DCA], which might be expected from the possibility of forming strong hydrogen bonds between the amino group on [MAT]$^+$ and the lone pairs in one or more nitrogen atoms of [DCA]$^-$.

IV. CONCLUSIONS

Nanoparticulate boron powder dispersed in, and capped with, two different hypergolic ILs was synthesized using a ball milling technique. We have shown that the boron nanoparticles produced through this process are capped by IL layers that are dense enough to protect the boron surfaces from air oxidation. The combination of XPS, IR, and zeta potential results suggest that binding by [MAT]$^+$ is dominant when it is present, probably involving a B−N bond. However, in [BMIM][DCA] there is also a strongly bound layer, despite the fact that neither [BMIM]Cl nor Na[DCA] binds. We suggest that this [BMIM][DCA] involves cooperative binding of the cation and anion, with some indication from the zeta potential that anion binding predominates. The differences in binding of [MAT][DCA] and [MAT]I suggest that binding is cooperative in those systems as well. TGA measurements show that the IL bound to the nanoparticles decomposes at lower temperatures compared to the neat ILs. Surface coverage calculations confirmed the conclusion from XPS and IR that the capping layer for [MAT][DCA] is substantially thicker (at least ∼3 times thicker) than that formed by [BMIM][DCA]. This research shows the potential importance of organic substituents

in tailoring the desired specific surface interactions with metal nanoparticles.

While our data provide considerable insight into factors that influence formation of an effective IL capping layer, and data that would sensitively test models of IL–boron binding, true atomic-level detail regarding the IL–surface binding mechanism is not likely to come from experiments. For this reason, a theoretical study of the nature of IL–surface binding would be quite valuable.

■ ASSOCIATED CONTENT

ⓢ Supporting Information
Additional XPS and TGA data. Detailed calculations of IL coverage of nanoparticles. This material is available free of charge via the Internet at http://pubs.acs.org.

■ AUTHOR INFORMATION

Corresponding Author
*E-mail: anderson@chem.utah.edu.

Notes
The authors declare no competing financial interest.
‖Senior Author.

■ ACKNOWLEDGMENTS

■ REFERENCES

(1) Clark, J. D. *Ignition! An Informal History of Liquid Rocket Propellants*; Rutgers University Press: New Brunswick, NJ, 1972.
(2) Cardulla, F. *J. Chem. Educ.* **1983**, *60*, 505–508.
(3) MacEwen, J. D.; Vernot, E. H. *Toxic Hazards Research Unit Annual Technical Report: 1977*; University of California: Irvine: Dayton, OH, September, 1977.
(4) Renner, R. *Environ. Sci. Technol.* **2001**, *35*, 410A–413A.
(5) Magee, J. W.; Kabo, G. J.; Frenkel, M. In *Physical Property Measurements and a Comprehensive Data Retrieval System for Ionic Liquids*, 226th ACS National Meeting, New York, NY.
(6) Yang, Q.; Dionysiou, D. D. *J. Photochem. Photobiol. A: Chem.* **2004**, *165*, 229–240.
(7) Visser, A. E.; Swatloski, R. P.; Reichert, W. M.; Mayton, R.; Sheff, S.; Wierzbicki, A.; Davis, J. H.; Rogers, R. D. *Environ. Sci. Technol.* **2002**, *36*, 2523–2529.
(8) Welton, T. *Chem. Rev.* **1999**, *99*, 2071–2083.
(9) Chauvin, Y.; Olivier-Bourbigou, H. *CHEMTECH* **1995**, *25*, 26–30.
(10) Ngo, H. L.; LeCompte, K.; Hargens, L.; McEwen, A. B. *Thermochim. Acta* **2000**, *357–358*, 97–102.
(11) Zhang, Y.; Gao, H.; Joo, Y.-H.; Shreeve, J. M. *Angew. Chem., Int. Ed.* **2011**, *50*, 9554–9562.
(12) Chambreau, S. D.; Schneider, S.; Rosander, M.; Hawkins, T.; Gallegos, C. J.; Pastewait, M. F.; Vaghjiani, G. L. *J. Phys. Chem. A* **2008**, *112*, 7816–7824.
(13) Hawkins, T. W.; Schneider, S.; Drake, G. W.; Vaghjiani, G.; Chambreau, S. *Hypergolic Fuels*, US Pat. 8,034,202 B1, 2011.
(14) Schneider, S.; Hawkins, T.; Ahmed, Y.; Rosander, M.; Hudgens, L.; Mills, J. *Angew. Chem., Int. Ed.* **2011**, *50*, 5886–5888.
(15) Schneider, S.; Hawkins, T.; Rosander, M.; Vaghjiani, G.; Chambreau, S.; Drake, G. *Energy Fuels* **2008**, *22*, 2871–2872.
(16) Zhang, Y.; Shreeve, J. n. M. *Angew. Chem., Int. Ed.* **2011**, *50*, 935–937.
(17) Huzel, D. K.; Huang, D. H. *Modern Engineering for Design of Liquid-Propellant Rocket Engines*; American Institute of Aeronautics and Astronautics, Inc.: Reston, VA, 1992.
(18) Xue, H.; Gao, Y.; Twamley, B.; Shreeve, J. M. *Chem. Mater.* **2005**, *17*, 191–198.
(19) Gao, Y.; Arritt, S. W.; Twamley, B.; Shreeve, J. M. *Inorg. Chem.* **2005**, *44*, 1704–1712.
(20) Jin, C.-M.; Ye, C. F.; Piekarski, C.; Twamley, B.; Shreeve, J. M. *Eur. J. Inorg. Chem.* **2005**, *2005*, 3760–3767.
(21) Xue, H.; Arritt, S. W.; Twamley, B.; Shreeve, J. M. *Inorg. Chem.* **2004**, *43*, 7972–7977.
(22) Xue, H.; Twamley, B.; Shreeve, J. M. *J. Mater. Chem.* **2005**, *15*, 3459–3465.
(23) Ye, C.; Xiao, J.-C.; Twamley, B.; Shreeve, J. M. *Chem. Commun.* **2005**, 2750–2752.
(24) *Energetic Materials: Part 1. Decomposition, Crystal and Molecular Properties*; Elsevier: Amsterdam, The Netherlands, 2003.
(25) Fried, L. E.; Manaa, M. R.; Pagoria, P. F.; Simpson, R. L. *Annu. Rev. Mater. Res.* **2001**, *31*, 291–321.
(26) Politzer, P.; Murray, J. S.; Seminario, J. M.; Lane, P.; Grice, M. E.; Concha, M. C. *J. Mol. Struct. (Theochem)* **2001**, *573*, 1–10.
(27) Rice, B. M.; Pai, S. V.; Hare, J. *Combust. Flame* **1999**, *118*, 445–458.
(28) Hammerl, A.; Hiskey, M. A.; Holl, G.; Klapötke, T. M.; Polborn, K.; Stierstorfer, J.; Weigand, J. J. *Chem. Mater.* **2005**, *17*, 3784–3793.
(29) Katritzky, A. R.; Singh, S.; Kirichenko, K.; Holbrey, J. D.; Smiglak, M.; Reichert, W. M.; Rogers, R. D. *Chem. Commun.* **2005**, 868–870.
(30) Katritzky, A. R.; Singh, S.; Kirichenko, K.; Smiglak, M.; Holbrey, J. D.; Reichert, W. M.; Spear, S. K.; Rogers, R. D. *Chem. Eur. J.* **2006**, *12*, 4630–4641.
(31) Pogodina, N. V.; Metwalli, E.; Müller-Buschbaum, P.; Wendler, K.; Lungwitz, R.; Spange, S.; Shamshina, J. L.; Rogers, R. D.; Friedrich, C. *J. Phys. Chem. Lett.* **2011**, *2*, 2571–2576.
(32) Smiglak, M.; Bridges, N. J.; Dilip, M.; Rogers, R. D. *Chemistry* **2008**, *14*, 11314–9.
(33) Xue, H.; Gao, Y.; Twamley, B.; Shreeve, J. M. *Inorg. Chem.* **2005**, *44*, 5068–5072.
(34) Xue, H.; Twamley, B.; Shreeve, J. M. *J. Mater. Chem.* **2005**, *15*, 3459–3465.
(35) Cox, J. D.; Wagman, D. D.; Medvedev, V. A. *CODATA Key Values for Thermodynamics*; Hemisphere Publishing Corp: New York, 1984.
(36) Hsia, H. T.-S. *Air-Augmented Combustion of Boron and Boron-Metal Alloys*; Air Force Rocket Propulsion Laboratory, Air Force Systems Command, United States Air Force: Edwards, CA, 1971.
(37) Jain, A.; Anthonysamy, S.; Ananthasivan, K.; Gupta, G. S. *Thermochim. Acta* **2010**, *500*, 63–68.
(38) Jain, A.; Joseph, K.; Anthonysamy, S.; Gupta, G. S. *Thermochim. Acta* **2011**, *514*, 67–73.
(39) Kuo, K. K.; Risha, G. A.; Evans, B. J.; Boyer, E. *Mater. Res. Soc. Symp. Proc.* **2004**, 3–14.
(40) Mitani, T.; Izumikawa, M. *J. Spacecr. Rockets* **1991**, *28*, 78–84.
(41) Risha, G. A.; Boyer, E.; Evans, B.; Kuo, K. K.; Malek, R. *Mater. Res. Soc. Symp. Proc.* **2003**, *800*, 243–254.

(42) Young, G. *Metallic Nanoparticles as Fuel Additives in Airbreathing Combustion*; University of Maryland, Digital Repository at the University of Maryland, 2007.

(43) Hsieh, W.-H.; Peretz, A.; Huang, I.-T.; Kuo, K. K. *J. Propulsion* **1991**, *7*, 497−503.

(44) Van Devener, B.; Perez, J. P. L.; Anderson, S. L. *J. Mater. Res.* **2009**, *24*, 3462−3464.

(45) Van Devener, B.; Perez, J. P. L.; Jankovich, J.; Anderson, S. L. *Energy Fuels* **2009**, *23*, 6111−6120.

(46) Perez, J. P. L.; McMahon, B. W.; Anderson, S. L. *J. Propul. Power* **2013**, DOI: 10.2514/1.B34724.

(47) McCrary, P. D.; Beasley, P. A.; Cojocaru, O. A.; Schneider, S.; Hawkins, T. W.; Perez, J. P. L.; McMahon, B. W.; Pfeil, M.; Boatz, J. A.; Anderson, S. L.; Son, S. F.; Rogers, R. D. *Chem. Commun.* **2012**, *48*, 4311−4313.

(48) Wagner, C. D.; Naumkin, A. V.; Kraut-Vass, A.; Allison, J. W.; Powell, C. J.; John, R. Rumble, J. *NIST X-ray Photoelectron Spectroscopy Database*, June 6, 2000 ed.; Measurement Services Division of the National Institute of Standards and Technology (NIST) Material Measurement Laboratory (MML): Maryland, 2007.

(49) Perdew, J. P.; Adrienn, R.; Csonka, G. I.; Constantin, L. A.; Sun, J. *Phys. Rev. Lett.* **2009**, *103*, 026403.

(50) Krishnan, R.; Binkley, J. S.; Seeger, R.; Pople, J. A. *J. Chem. Phys.* **1980**, *72*, 650−654.

(51) Hariharan, P. C.; Pople, J. A. *Theor. Chim. Acta.* **1973**, *28*, 213−222.

(52) Clark, T.; Chandrasekhar, J.; Spitznagel, G. W.; Schleyer, P. v. R. *J. Comput. Chem.* **1983**, *4*, 294−301.

(53) Schmidt, M. W.; Baldridge, K. K.; Boatz, J. A.; Elbert, S. T.; Gordon, M. S.; Jensen, J. H.; Koseki, S.; Matsunaga, N.; Nguyen, K. A.; Su, S. *J. Comput. Chem.* **1993**, *14*, 1347−1363.

(54) Gordon, M. S.; Schmidt, M. W. *Advances in Electronic Structure Theory: GAMESS a Decade Later. In Theory and Applications of Computational Chemistry: The First Forty Years*; Elsevier: Amsterdam, 2005.

(55) Phillips, J. *Phys. Rev.* **1961**, *123*, 420−424.

(56) Smith, E. F.; Garcia, I. J.; Briggs, D.; Licence, P. *Chem. Commun. (Cambridge, U. K.)* **2005**, 5633−5.

(57) Smith, E. F.; Rutten, F. J. M.; Villar-Garcia, I. J.; Briggs, D.; Licence, P. *Langmuir* **2006**, *22*, 9386−9392.

(58) Hurisso, B. B.; Lovelock, K. R.; Licence, P. *Phys. Chem. Chem. Phys.* **2011**, *13*, 17737−48.

(59) Zhang, H.; Cui, H. *Langmuir* **2009**, *25*, 2604−2612.

(60) Zhang, Q.; Ma, X.; Liu, S.; Yang, B.; Lu, L.; He, Y.; Deng, Y. *J. Mater. Chem.* **2011**, *21*, 6864.

(61) Lovelock, K. R.; Kolbeck, C.; Cremer, T.; Paape, N.; Schulz, P. S.; Wasserscheid, P.; Maier, F.; Steinrück, H.-P. *J. Phys. Chem. B* **2009**, *113*, 2854−2864.

(62) Zhou, X.-L.; Blass, P. M.; Koel, B. E.; White, J. M. *Surf. Sci.* **1992**, *271*, 452−467.

(63) Moulder, J. F.; Stickle, W. F.; Sobol, P. E.; Bomben, K. D.; *Handbook of X-ray Photoelectron Spectroscopy*; Perkin-Elmer Corporation: Eden Prairie, MN, 1992.

(64) Balakrishnarajan, M. M. *J. Am. Chem. Soc.* **2004**, *126*, 13119−13131.

(65) Carvalho, P. J.; Regueira, T.; Santos, L. M. N. B. F.; Fernandez, J.; Coutinho, J. A. P. *J. Chem. Eng. Data* **2010**, *55*, 645−652.

(66) Niedermaier, I.; Kolbeck, C.; Taccardi, N.; Schulz, P. S.; Li, J.; Drewello, T.; Wasserscheid, P.; Steinrück, H.-P.; Maier, F. *ChemPhysChem* **2012**, *13*, 1725−1735.

(67) Powell, C. J.; Jablonski, A. *NIST Electron Effective Attenuation Length Database*, 2003.

(68) Trehan, R.; Lifshitz, Y.; Rabalais, J. W. *J. Vac. Sci. Technol. A* **1990**, *8*, 4026−4032.

(69) Neouze, M.-A. *J. Mater. Chem.* **2010**, *20*, 9593−9607.

(70) Dupont, J.; Scholten, J. D. *Chem. Soc. Rev.* **2010**, *39*, 1790−1804.

(71) Khare, V.; Kraupner, A.; Mantion, A.; Jelicic, A.; Thunemann, A. F.; Giordano, C.; Taubert, A. *Langmuir* **2010**, *26*, 10600−5.

(72) Fonseca, G. S.; Machado, G.; Teixeira, S. R.; Fecher, G. H.; Morais, J.; Alves, M. C.; Dupont, J. *J. Colloid Interface Sci.* **2006**, *301*, 193−204.

(73) Ott, L. S.; Cline, M. L.; Deetlefs, M.; Seddon, K. R.; Finke, R. G. *J. Am. Chem. Soc.* **2005**, *127*, 5758−5759.

(74) Schrekker, H. S.; Gelesky, M. A.; Stracke, M. P.; Schrekker, C. M.; Machado, G.; Teixeira, S. R.; Rubim, J. C.; Dupont, J. *J. Colloid Interface Sci.* **2007**, *316*, 189−95.

(75) Mendonça, A. C. F.; Malfreyt, P.; Pádua, A. A. H. *J. Chem. Theory Comput.* **2012**, *8*, 3348−3355.

(76) Hendrickson, D. N.; Hollander, J. M.; Jolly, W. L. *Inorg. Chem.* **1969**, *8*, 2642−2647.

(77) Jagoda-Cwiklik, B.; Wang, X.-B.; Woo, H.-K.; Yang, J.; Wang, G.-J.; Zhou, M.; Jungwirth, P.; Wang, L.-S. *J. Phys. Chem. A* **2007**, *111*, 7719−7725.

(78) Peláez, R. J.; Blondel, C.; Delsart, C.; Drag, C. *J. Phys. B: At., Mol. Opt. Phys.* **2009**, *42*, 125001.

(79) Lotsch, B. V.; Senker, J.; Kockelmann, W.; Schnick, W. *J. Solid State Chem.* **2003**, *176*, 180−191.

(80) Kester, D. J.; Ailey, K. S.; Davis, R. F. *J. Mater. Res.* **1993**, *8*, 1231−1216.

(81) Verinaud, F.; Weissmantel, E.; Grenier, I.; Celerier, A.; Machet, J. *Thin Solid Films* **1992**, *209*, 59−66.

(82) McCrary, P. D.; Beasley, P. A.; Kelley, S. P.; Schneider, S.; Boatz, J. A.; Hawkins, T. W.; Perez, J. P. L.; McMahon, B. W.; Pfiel, M.; Son, S. F.; Anderson, S. L.; Rogers, R. D. *Phys. Chem. Chem. Phys.* **2012**, *14*, 13194−13198.

(83) Delgado, A. V.; González-Caballero, F.; Hunter, R. J.; Koopal, L. K.; Lyklema, J. *Measurement and Interpretation of Electrokinetic Phenomena (IUPAC Technical Report). Pure Appl. Chem.* **2005**, *77*, 1753−1805.

(84) Attard, P.; Antelmi, D.; Larson, I. *Langmuir* **2000**, *16*, 1542−1552.

(85) Paraknowitsch, J. P.; Zhang, J.; Su, D.; Thomas, A.; Antonietti, M. *Adv. Mater.* **2010**, *22*, 87−92.

(86) Wooster, T. J.; Johanson, K. M.; Fraser, K. J.; MacFarlane, D. R.; Scott, J. L. *Green Chem.* **2006**, *8*, 691−696.

(87) Weast, R. C.; Astle, M. J.; Beyer, W. H. *CRC Handbook of Chemistry and Physics*, 66 ed.; CRC Press: Boca Raton, 1985.

(88) Lowdin, P. O. *Adv. Quantum Chem.* **1970**, *5*, 185−199.

(89) Mulliken, R. S. *J. Chem. Phys.* **1955**, *23*, 1841.

(90) Mulliken, R. S. *J. Chem. Phys.* **1955**, *23*, 2338.

(91) Mulliken, R. S. *J. Chem. Phys.* **1955**, *23*, 2343.